Report

SOURCE DATA | TRANSPARENT PROCESS | OPEN ACCESS

EMBO reports

Loss of enteric neuronal *Ndrg4* promotes colorectal cancer via increased release of Nid1 and Fbln2

Nathalie Vaes[1], Simone L Schonkeren[1], Glenn Rademakers[1], Amy M Holland[1], Alexander Koch[1], Marion J Gijbels[1,2,3], Tom G Keulers[4], Meike de Wit[5,6], Laura Moonen[1], Jaleesa R M Van der Meer[1], Edith van den Boezem[1], Tim G A M Wolfs[7], David W Threadgill[8,9], Jeroen Demmers[10], Remond J A Fijneman[6], Connie R Jimenez[5], Pieter Vanden Berghe[11], Kim M Smits[1], Kasper M A Rouschop[4], Werend Boesmans[1,12], Robert M W Hofstra[13] & Veerle Melotte[1,13,*]

Abstract

The N-Myc Downstream-Regulated Gene 4 (*NDRG4*), a prominent biomarker for colorectal cancer (CRC), is specifically expressed by enteric neurons. Considering that nerves are important members of the tumor microenvironment, we here establish different *Ndrg4* knockout (*Ndrg4*$^{-/-}$) CRC models and an indirect co-culture of primary enteric nervous system (ENS) cells and intestinal organoids to identify whether the ENS, via NDRG4, affects intestinal tumorigenesis. Linking immunostainings and gastrointestinal motility (GI) assays, we show that the absence of *Ndrg4* does not trigger any functional or morphological GI abnormalities. However, combining *in vivo*, *in vitro*, and quantitative proteomics data, we uncover that *Ndrg4* knockdown is associated with enlarged intestinal adenoma development and that organoid growth is boosted by the *Ndrg4*$^{-/-}$ ENS cell secretome, which is enriched for Nidogen-1 (Nid1) and Fibulin-2 (Fbln2). Moreover, NID1 and FBLN2 are expressed in enteric neurons, enhance migration capacities of CRC cells, and are enriched in human CRC secretomes. Hence, we provide evidence that the ENS, via loss of *Ndrg4*, is involved in colorectal pathogenesis and that ENS-derived Nidogen-1 and Fibulin-2 enhance colorectal carcinogenesis.

Keywords colorectal cancer; enteric nervous system; Fibulin-2; Ndrg4; Nidogen-1

Subject Categories Cancer; Neuroscience; Signal Transduction

DOI 10.15252/embr.202051913 | Received 16 October 2020 | Revised 9 March 2021 | Accepted 11 March 2021 | Published online 23 April 2021

EMBO Reports (2021) 22: e51913

Introduction

Colorectal cancer (CRC) is one of the most common lethal malignancies in the world even with major advances in screening and therapeutic strategies. This is partly attributed to the incomplete knowledge regarding the pathogenesis of CRC. Notably, it is well established that CRC not only arises from (epi-)genetic events in epithelial cells, since also cells and signals from the tumor microenvironment (TME) have been highlighted to be important for the initiation and progression of CRC (Colangelo *et al*, 2017).

Several cell types within the gastrointestinal (GI) tract, e.g., fibroblast, immune, nerve, and endothelial cells, constitute the TME. Even though the significant impact of immune cells on (colorectal) carcinogenesis has been recognized for several years (Gutting *et al*, 2018), research into other TME components is still in its infancy. Interest in the role of the nervous system in tumorigenesis recently took the foreground (Venkatesh, 2019; Zahalka & Frenette, 2020) with the publication of several landmark papers describing the functional importance of nerves in skin (Peterson *et al*, 2015),

1 Department of Pathology, GROW–School for Oncology and Developmental Biology, Maastricht University Medical Center, Maastricht, The Netherlands
2 Department of Molecular Genetics, Cardiovascular Research Institute Maastricht (CARIM), Maastricht, The Netherlands
3 Department of Medical Biochemistry, Academic Medical Center, Amsterdam, The Netherlands
4 Department of Radiotherapy, GROW-School for Oncology and Developmental Biology and Comprehensive Cancer Center Maastricht MUMC+, Maastricht University, Maastricht, The Netherlands
5 Department of Medical Oncology and Oncoproteomics Laboratory, Cancer Center Amsterdam, Vrije Universiteit Amsterdam, Amsterdam UMC, Amsterdam, The Netherlands
6 Department of Pathology, Netherlands Cancer Institute, Amsterdam, The Netherlands
7 Department of Pediatrics, GROW-School for Oncology and Developmental Biology, Maastricht University, Maastricht, The Netherlands
8 Department of Molecular and Cellular Medicine, Texas A&M University Health Science Center, College Station, TX, USA
9 Department of Biochemistry and Biophysics, Texas A&M University, College Station, TX, USA
10 Proteomics Center, Erasmus University Medical Center, Rotterdam, The Netherlands
11 Laboratory for Enteric Neuroscience (LENS) and Translational Research Center for Gastrointestinal Disorders (TARGID), Department of Chronic Diseases, Metabolism and Ageing, KU Leuven, Leuven, Belgium
12 Biomedical Research Institute (BIOMED), Hasselt University, Hasselt, Belgium
13 Department of Clinical Genetics, Erasmus University Medical Center, Rotterdam, The Netherlands
*Corresponding author. Tel: +31 43 3872210; Fax: +31 43 3876613; E-mail: veerle.melotte@maastrichtuniversity.nl

prostate (Ayala *et al,* 2008; Magnon *et al,* 2013), breast (Kamiya *et al,* 2019), pancreatic (Bapat *et al,* 2011; Stopczynski *et al,* 2014), and gastric (Zhao *et al,* 2014; Hayakawa *et al,* 2017) cancer. These studies showed that surgical or pharmacological denervation of autonomic or (para-) sympathetic nerves suppresses cancer development. Remarkably, even with perineural invasion and neoneurogenesis being recognized as unfavorable prognostic factors in CRC (Albo *et al,* 2011; Knijn *et al,* 2016), knowledge regarding the contribution of the intrinsic nervous system of the gut: the enteric nervous system (ENS (Furness, 2012)) to CRC is sparse (Rademakers *et al,* 2017; Duchalais *et al,* 2018). The ENS is a complex neuroglial network embedded in the gut wall along the entire digestive tract. It communicates with other intestinal cells by transmitting signals like neurotransmitters, (neuro-) peptides, and hormones, in order to orchestrate GI functions (e.g., intestinal motility, blood flow and intestinal epithelial barrier integrity) and to maintain GI homeostasis (Furness, 2012). The importance of the ENS is highlighted by the wide range of enteric neuropathies (e.g., Hirschsprung disease) and inflammatory conditions that may arise from defective ENS development and/or functioning (Obermayr *et al,* 2013; Margolis & Gershon, 2016) and depicts some potential importance in colorectal carcinogenesis (Rademakers *et al,* 2017).

Previously, we revealed that the N-Myc Downstream-Regulated Gene 4 (*NDRG4*), one of the most accurate DNA methylation-based biomarkers for the early detection of CRC (Melotte *et al,* 2009; Imperiale *et al,* 2014), is specifically expressed in the ENS (Vaes *et al,* 2017; Vaes *et al,* 2018). Even though *NDRG4* is an established DNA methylation-based biomarker (Melotte *et al,* 2009; Imperiale *et al,* 2014), knowledge regarding its functional importance is sparse, yet seems to affect key developmental and carcinogenic processes, including cellular proliferation and differentiation (Melotte *et al,* 2010; Vaes *et al,* 2018; Schonkeren *et al,* 2019). Moreover, Ndrg4 has been shown to be involved in vesicle trafficking and thus possibly secretory actions (Benesh *et al,* 2013; Fontenas *et al,* 2016). Given the extensive crosstalk between the ENS and the intestinal epithelium, we here investigate whether enteric neuronal NDRG4 influences the intestinal (tumor) epithelium.

Results and Discussion

Loss of *Ndrg4* has no major influence on intestinal morphology and physiology

Prior to addressing the role of *Ndrg4* in CRC, we sought to explore its overall impact in the intestinal tract. Therefore, we first performed in-depth histological analyses of intestinal segments of $Ndrg4^{-/-}$ and $Ndrg4^{+/+}$ mice. Focusing on the epithelial cell layer, these analyses revealed a normal intestinal epithelial architecture: i.e., uniform presence of alkaline phosphatase in the enterocyte brush border and a similar number and distribution of Paneth cells (Lysozyme; $P = 0.537$) in the small intestine, and of neuroendocrine (chromogranin A; $P = 0.304$), goblet (PAS; $P = 0.958$), and proliferating cells (Ki67; $P = 0.543$) in the colon (Fig 1A). Within the small intestine, we observed comparable numbers and distributions of neuroendocrine, goblet, and proliferating cells (Fig EV1A–C). The number of Lgr5-positive cells detected within small and large intestinal segments (Fig EV1D and E) were similar as previously described (Dehmer *et al,* 2011; Fernandez Vallone *et al,* 2020). However, no differences in the number of Lgr5-positive cells were observed between $Ndrg4^{+/+}$ and $Ndrg4^{-/-}$ intestines.

The organization of the ENS was evaluated by antibody labeling for the neuron-specific class III beta-tubulin (Tuj1) and the S100 calcium-binding protein (S100). As shown in Fig 1B, this labeling did not reveal structural or organizational differences of the colonic myenteric plexus between $Ndrg4^{+/+}$ and $Ndrg4^{-/-}$ mice ($n = 3$). Labeling with the pan-neuronal marker HuC/D showed that the density of enteric neurons in the myenteric plexus of the proximal and distal colon was similar between $Ndrg4^{-/-}$ and $Ndrg4^{+/+}$ mice (Fig 1C and D, $P = 0.906$ and $P = 0.811$, respectively). Finally, also anti-PGP9.5 immunohistochemistry did not reveal any differences in the mucosal innervation of the small and large intestine of $Ndrg4^{-/-}$ and $Ndrg4^{+/+}$ mice (Fig EV2).

Even though loss of *Ndrg4* did not impact intestinal morphology, we further assessed whether *Ndrg4* knockdown affects intestinal physiology. Gastrointestinal motor activity was analyzed by determining the whole-gut and small intestinal transit using non-absorbable carmine red solution and colonic motility through assessment of the colonic propulsion of a glass bead. Consistent with their similar whole-gut transit time (Fig 1E; 194.3 min versus 149.5 min, $P = 0.128$), $Ndrg4^{+/+}$ and $Ndrg4^{-/-}$ mice excreted a similar number of fecal pellets within the first hour of the assay (Mean of 7.60 versus 6.00 pellets, $P = 0.276$), with a similar weight and stool water content (Fig 1F; mean of 19.24 mg versus 18.14 mg, $P = 0.665$; Fig 1G; mean of 60.48% versus 64.34%, $P = 0.328$). Similarly, we did not observe statistically significant differences in the small intestinal transit (Fig 1H; 52.4% versus 71.7%, $P = 0.094$) or colonic propulsion (Fig 1I; 299.0 s versus 246.9 s, $P = 0.449$) between $Ndrg4^{+/+}$ and $Ndrg4^{-/-}$ mice. Together these data indicate that loss of *Ndrg4* has no major effects on intestinal morphology and physiology in healthy conditions.

Deletion of *Ndrg4* enhances intestinal adenoma growth

Consequently, the influence of *Ndrg4* on CRC was studied during colorectal carcinogenesis using a genetic ($APC^{Min/+}$) (Heyer *et al,* 1999) and azoxymethane (AOM)-induced (Neufert *et al,* 2007) model. In both models, $Ndrg4^{-/-}$ mice are similar to $Ndrg4^{+/+}$ mice with respect to their physical appearance and body weight (Fig 2A and B, $P_{APC^{Min/+}}=0.802$, $P_{AOM} = 0.352$). The homozygous deletion of *Ndrg4* did not change the tumor incidence in the small intestine of $APC^{Min/+}$ mice (Fig 2C, $P = 0.764$) nor in the colon of AOM-treated mice (Fig 2D, $P = 0.903$). However, the adenomas in the small intestine of $Ndrg4^{-/-}$-$APC^{Min/+}$ mice and in the colon of AOM-treated $Ndrg4^{-/-}$ mice were significantly enlarged compared to those of $Ndrg4^{+/+}$-$APC^{Min/+}$ mice (Fig 2E–G, $P = 0.008$) and AOM-treated $Ndrg4^{+/+}$ mice (Fig 2F–H, $P = 0.043$). Moreover, the small intestinal adenomas of $Ndrg4^{-/-}$-$APC^{Min/+}$ mice and colonic adenomas of AOM-treated $Ndrg4^{-/-}$ mice were characterized by higher levels of an aggressiveness marker: i.e., a non-statistically significantly higher mean nuclear β-catenin immunoreactivity ($APC^{min/+}$=15.28 ± 2.75; AOM = 44.84 ± 13.11), than adenomas of $Ndrg4^{+/+}$-$APC^{Min/+}$ (8.90 ± 1.64) and AOM-treated $Ndrg4^{+/+}$ (16.34 ± 4.74) mice, respectively ($p_{APC^{Min/+}}=0.060$; $p_{AOM} = 0.085$ (Wong *et al,* 2004)). The more aggressive phenotype of intestinal adenomas in $Ndrg4^{-/-}$ mice reflects the human situation, where de-differentiated tumor cells with

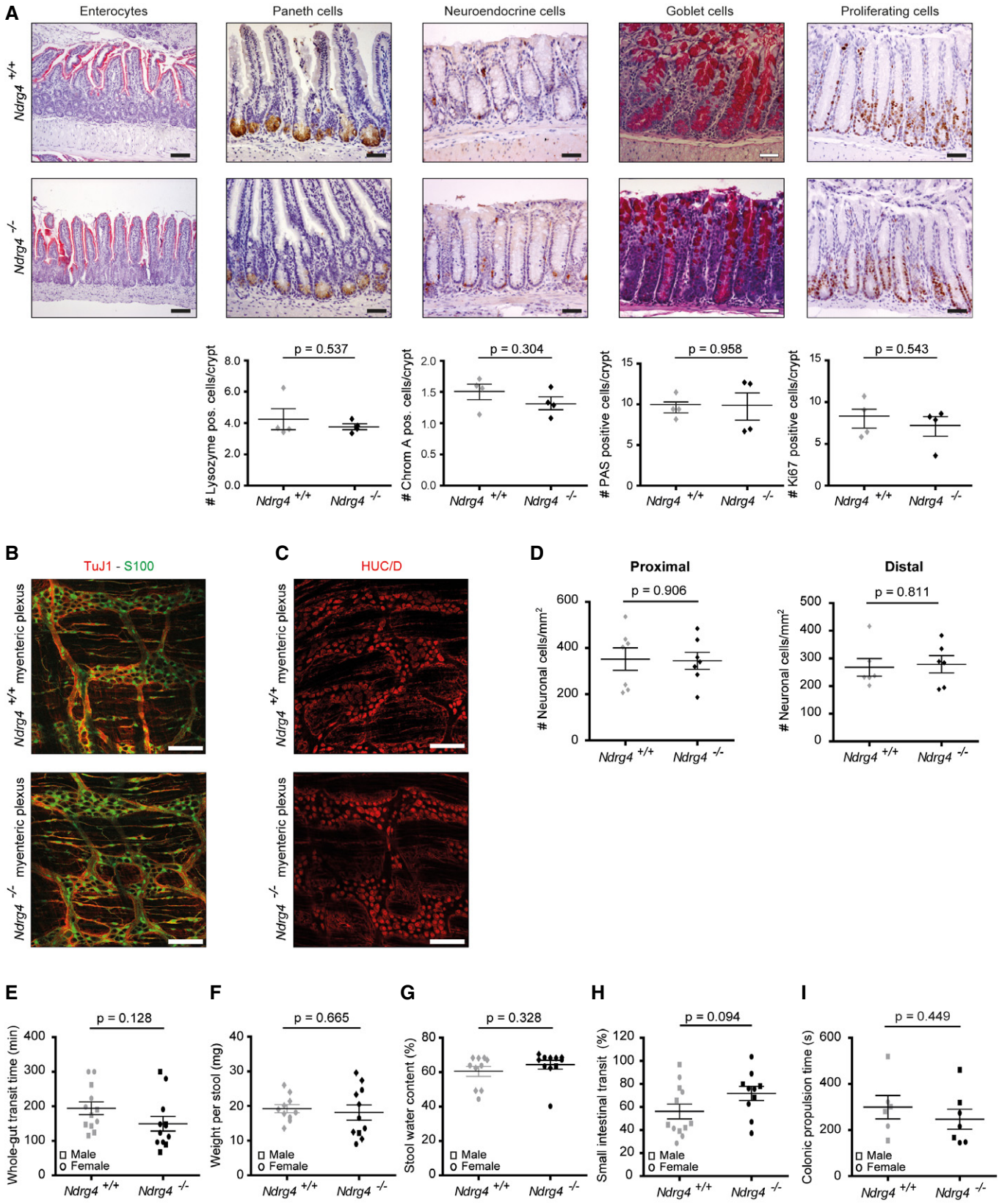
A
Enterocytes
Paneth cells
Neuroendocrine cells
Goblet cells
Proliferating cells
Ndrg4 +/+
Ndrg4 -/-
# Lysozyme pos. cells/crypt
p = 0.537
# Chrom A pos. cells/crypt
p = 0.304
# PAS positive cells/crypt
p = 0.958
# Ki67 positive cells/crypt
p = 0.543
B
TuJ1 - S100
myenteric plexus
C
HUC/D
D
Proximal
p = 0.906
Distal
p = 0.811
# Neuronal cells/mm2
E
p = 0.128
Whole-gut transit time (min)
F
p = 0.665
Weight per stool (mg)
G
p = 0.328
Stool water content (%)
H
p = 0.094
Small intestinal transit (%)
I
p = 0.449
Colonic propulsion time (s)
Male
Female

Figure 1.

Figure 1. Loss of *Ndrg4* does not alter intestinal morphology or physiology.

A Representative microscopic views of $Ndrg4^{+/+}$ and $Ndrg4^{-/-}$ murine intestinal sections (n = 4, 12 months of age) reveal an even distribution of alkaline phosphatase along the enterocyte brush border, and a similar number and distribution of Paneth cells (Lysozyme) in the small intestine; and neuroendocrine (chromogranin A), goblet (PAS+), and proliferating (Ki67) cells in the colon. Scale bars, 50 μm.

B, C Representative microscopic views of the myenteric plexus of $Ndrg4^{+/+}$ and $Ndrg4^{-/-}$ murine colonic sections labeled with either TuJ1 and S100 (B, n = 3) or HuC/D (C, n = 6) did not reveal structural or organizational differences in the ganglionic network of $Ndrg4^{+/+}$ and $Ndrg4^{-/-}$ mice. Scale bars, 100 μm.

D Quantification of the enteric neuronal cell number (HuC/D) shows a similar number of enteric neurons in the proximal and distal colon of $Ndrg4^{+/+}$ and $Ndrg4^{-/-}$ mice (n = 6).

E–I Gastrointestinal motility assays reveal a similar whole-gut transit time (E; n = 12 versus 12), with a similar weight per stool and stool water content of the fecal pellets (F, G; n = 11 versus 10), a comparable small intestinal transit (H; n = 10 versus 12) and colonic propulsion time (I; n = 7 versus 6) in $Ndrg4^{-/-}$ compared to $Ndrg4^{+/+}$ mice.

Data information: All data are presented as mean ± SEM, with P-values determined using a two-tailed, unpaired t-test.

increased nuclear β-catenin levels are known to have aggressive morphological features, which is associated with a poor prognosis (Wong *et al,* 2004). Interestingly, while AOM treatment normally mainly induces colonic adenoma formation (Neufert *et al,* 2007), 83.3% (10/12) of the AOM-treated $Ndrg4^{-/-}$ mice also developed small intestinal adenomas compared to just 31.1% (5/16) of $Ndrg4^{+/+}$ mice (P = 0.019).

Even though intestinal expression of Ndrg4 is limited to the ENS (Vaes *et al,* 2017), we have to keep in mind that in this constitutive *Ndrg4* knockout model, not only enteric neurons, but also peripheral nerves are deficient for *Ndrg4*. Given that extrinsic denervation can reduce carcinogenesis, as seen in other cancer types (Magnon *et al,* 2013; Stopczynski *et al,* 2014; Zhao *et al,* 2014), it may be speculated that *Ndrg4* deficiency in peripheral nerves could contribute to the observed phenotype. Moreover, we aimed to ensure that the above-described effects were not mediated by low or undetectable levels of *Ndrg4* in the intestinal epithelium using a conditional epithelial-specific *Ndrg4* knockdown model: i.e., $Ndrg4^{fl/fl}$-*VillinCre* mice crossed with $APC^{Min/+}$ mice. We observed that $Ndrg4^{fl/fl}$-*VillinCre*-$APC^{Min/+}$ and $Ndrg4^{fl/fl}$-$APC^{Min/+}$ mice have a comparable body weight (Fig 2I, P = 0.717) and developed an equal number of adenomas in their small intestine (Fig 2J, P = 0.730). In contrast to the observations in the constitutive knockout model, the epithelial-specific knockdown of *Ndrg4* did not alter the size (Fig 2K and L, P = 0.554) or aggressiveness ($Ndrg4^{fl/fl}$-*VillinCre*-$APC^{Min/+}$= 18.16 ± 1.45 versus $Ndrg4^{fl/fl}$-$APC^{Min/+}$=18.59 ± 2.34; P = 0.879) of the small intestinal adenomas, confirming that the observed effects in the constitutive $Ndrg4^{-/-}$ models are caused by loss of non-epithelial *Ndrg4*.

Medium from $Ndrg4^{-/-}$ ENS cultures enhances IEO growth and is enriched for Nidogen-1 and Fibulin-2

In view of the link between Ndrg4 and the vesicle-associated proteins Vamp3 (Benesh *et al,* 2013) and Rabac1 (Kim *et al,* 2012), and the role of *Ndrg4* in vesicle trafficking in peripheral nerve cells affecting, e.g., *Snap25* and *Vamp2* (Fontenas *et al,* 2016), we aimed to identify whether *Ndrg4* also affects vesicle transport within the ENS. For this purpose, we analyzed the RNA expression of genes of the (neuronal-specific) vesicle trafficking machinery in $Ndrg4^{-/-}$ and $Ndrg4^{+/+}$ ENS cultures. The absence of *Ndrg4* in ENS cultures generated from $Ndrg4^{-/-}$ murine intestinal tissues was verified using qRT–PCR and Western Blotting (Fig 3A and B). In addition, the specific deficiency of *Ndrg4* in enteric neurons (HuC/D positive cells) was confirmed by immunofluorescence labeling (Fig 3C). As shown in Fig 3D, we tested the effect of *Ndrg4* knockdown in primary murine ENS cell cultures on several genes involved in (i) vesicle formation: *Rabac1* and *Nsf*, (ii) vesicle docking and fusion: *Vamp2*, *Snap25*, *Stx1a,* and *Rab3a*, and (iii) exocytotic release: *Stxbp1*, *Caly,* and *Cadps*. A significantly reduced expression of *Rabac1* (78.3%, P = 0.016), *Stxbp1* (18.3%, P = 0.032), and *Caly* (82.1%, P = 0.029) was observed in $Ndrg4^{-/-}$ ENS cultures. This suggests that *Ndrg4* also modulates the vesicle trafficking machinery and potentially the subsequent secretion of soluble factors in enteric neurons.

To examine whether loss of *Ndrg4* actually induces differences in soluble/secreted factors, we exposed wild-type intestinal epithelial organoids (IEOs) to medium derived from $Ndrg4^{+/+}$ and $Ndrg4^{-/-}$ ENS cultures via a transwell membrane (Fig 3E–H) and evaluated the composition of the medium derived from $Ndrg4^{+/+}$ and $Ndrg4^{-/-}$ cells (Fig 4). IEOs exposed to $Ndrg4^{-/-}$ ENS culture medium display characteristic growth differences compared to IEOs stimulated with $Ndrg4^{+/+}$ ENS culture medium: i.e., their relative growth rate was enhanced even as the formation of new crypt buds per IEO (Fig 3E, P = 0.040 and Fig 3F, P = 0.014). Despite that IEOs exposed to either $Ndrg4^{+/+}$ or $Ndrg4^{-/-}$ ENS culture medium evolve through all growth stages (Fig 3G, i.e., from crypt to (entero-) sphere, budding enterosphere, enteroid, and microadenoma-like structure (Lorenzi *et al,* 2016)), IEOs exposed to $Ndrg4^{-/-}$ ENS culture medium expand more rapidly and therefore already develop into a

Figure 2. Enhanced intestinal adenoma progression in $Ndrg4^{-/-}$ mice crossed with $APC^{Min/+}$ mice (A, C, E, G) or treated with azoxymethane (AOM; B, D, F, H), but not after epithelial loss of *Ndrg4* (I–L).

A, B $Ndrg4^{+/+}$ and $Ndrg4^{-/-}$ mice have a similar bodyweight (n = 17 versus 14 in (A) and n = 25 versus 19 in (B).

C, D The total number of small intestinal (SI) and colonic adenomas that develops remains the same after deletion of *Ndrg4* (n = 18 versus 15 in (C) and n = 25 versus 19 in (D)).

E–H $Ndrg4^{-/-}$ mice develop significantly enlarged small intestinal (SI) polyps (E, G) and colon adenomas (F, H). N = 10 versus 13 in (E) and n = 20 versus 17 in (F).

I–L In contrast, $Ndrg4^{fl/fl}$ and $Ndrg4^{fl/fl}$-*VillinCre* mice have a similar bodyweight (I) and develop an equal number of adenomas (J) with an equivalent diameter (K, L). N = 13 versus 12 in (I), n = 13 versus 11 in (J) and n = 10 versus 8 in (K).

Data information: All data are presented as mean ± SEM with P-values determined using a two-tailed, unpaired t-test. Scale bars in (G, H, L), 50 μm. Intestinal adenomas are delineated with a blue dotted line in (G, H, L).

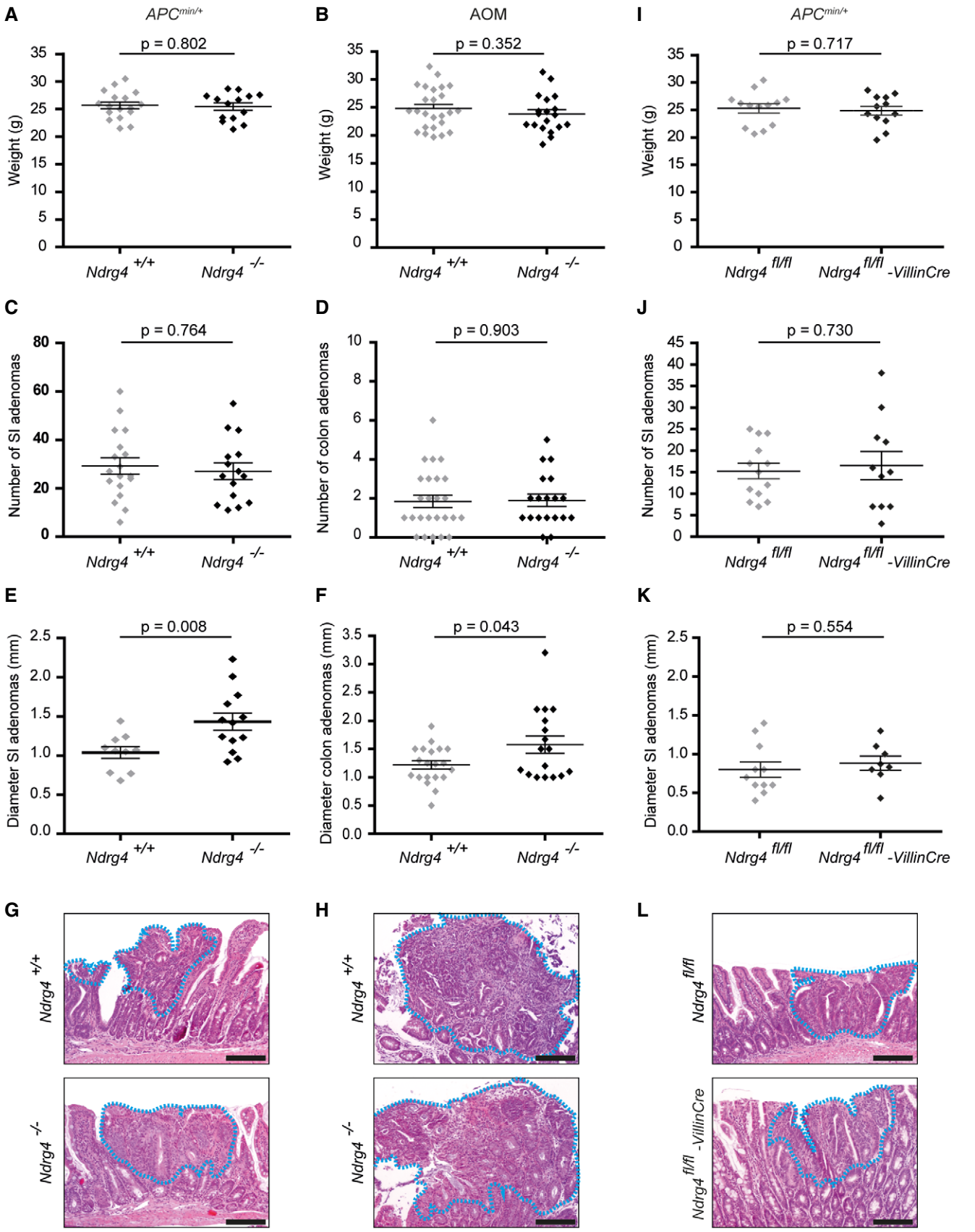

Figure 2.

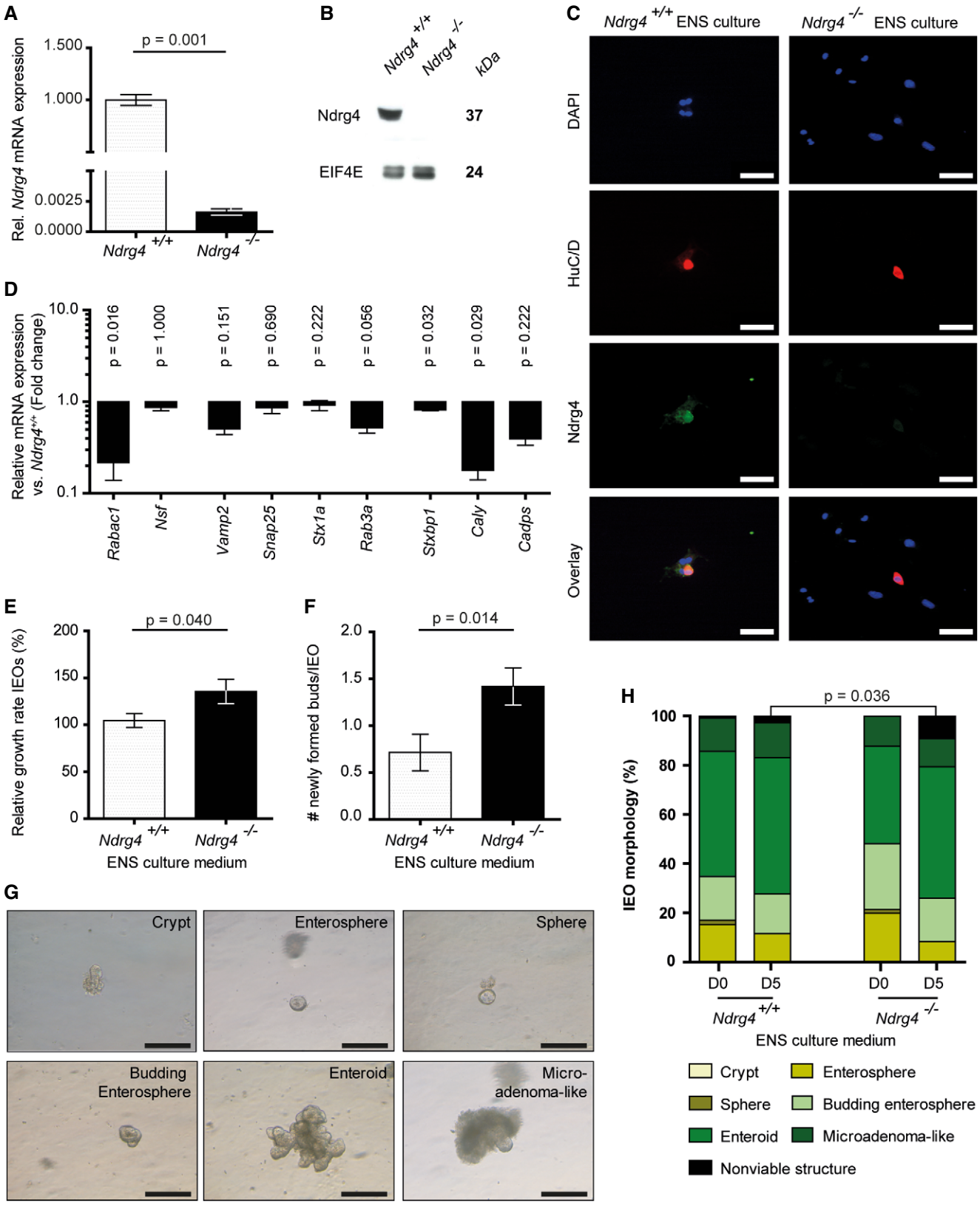

Figure 3.

Figure 3. Medium derived from *Ndrg4*$^{-/-}$ ENS cultures boosts organoid development.

A–C Relative *Ndrg4* mRNA (A) and Ndrg4 protein expression by Western blotting (B) and immunofluorescence (C) confirms the absence of Ndrg4 in enteric neurons of *Ndrg4*$^{-/-}$ mice (n = 3). EIF4E is used as a loading control in (B).

D qRT–PCR analysis of the *Ndrg4*$^{+/+}$ and *Ndrg4*$^{-/-}$ ENS cells used in the co-culture model showed that *Ndrg4*$^{-/-}$ ENS cultures have reduced levels of vesicle trafficking-related genes, with the expression of *Rabac1* (78.3%), *Nsf* (12.8%), *Vamp2* (49.2%), Snap25 (13.3%), *Stx1a* (8.0%), *Rab3a* (48.1%), *Stx1bp* (18.3%), *Caly* (82.1%), and *Cadps* (60.4%) being down-regulated in *Ndrg4*$^{-/-}$ ENS cultures compared to *Ndrg4*$^{+/+}$ ENS cultures. Data are derived from three independent experiments and log10-transformed ± SEM, with P-values determined using a Mann–Whitney U-test.

E, F Compared to *Ndrg4*$^{+/+}$ ENS-derived medium, addition of medium derived from *Ndrg4*$^{-/-}$ ENS cultures enhances the relative growth of intestinal epithelial organoids (E, IEOs) and accelerates the formation of new crypt buds per IEO in the course of 5 days (F).

G Medium from both *Ndrg4*$^{+/+}$ and *Ndrg4*$^{-/-}$ ENS cultures ensures IEO progression from crypt to (entero-) sphere, budding enterosphere, enteroid, and a microadenoma-like structure.

H After 5 days of culture, significantly more non-viable structures are formed upon influence of *Ndrg4*$^{-/-}$ ENS-derived medium.

Data information: The data represented in panel E-H are derived from three independent co-culture experiments with ± 35 IEOs per experimental condition. Data are shown as mean ± SEM (A, E, F). P-values are calculated using a two-tailed, unpaired t-test (A, E, F) or logistic regression (H). Scale bars in (C and G), 50 μm.

non-viable structure within 5 days (Fig 3H, 9.16% (12/131) versus 2.68% (3/112), P = 0.036). Together these data suggest that loss of *Ndrg4* in ENS cultures influences epithelial organoid growth through changes in the composition of the ENS-derived soluble/secreted fraction. Consequently, we assessed the composition of the secretomes of *Ndrg4*$^{+/+}$ and *Ndrg4*$^{-/-}$ ENS cultures by proteomics analysis (nanoLC-MS/MS). This analysis identified 1953 proteins of which only Nidogen-1 (Nid1) and Fibulin-2 (Fbln2), two extracellular matrix (ECM) molecules, were significantly enriched in the *Ndrg4*$^{-/-}$ compared to the *Ndrg4*$^{+/+}$ ENS cell secretome (Fig 4A, P = 0.0286 for both). We examined the gene expression of *Nid1* and *Fbln2* in the nervous system using the Mouse Brain atlas from the Linnarsson (Online resource: http://mousebrain.org/; Zeisel *et al,* 2018). Interestingly, *Nid1* and *Fbln2* are both found to be highly expressed within the ENS (Fig 4B), even though only a limited number of studies described that enteric neural crest cells produce and secrete ECM proteins (Akbareian *et al,* 2013; Nagy *et al,* 2018). The presence of these proteins in the ENS was confirmed using immunostainings as we found specific labeling within both myenteric and submucosal ganglia and interconnecting nerve fibers (Fig 4C–E), with a stronger intensity of both proteins in the *Ndrg4*$^{-/-}$ intestine than in the *Ndrg4*$^{+/+}$ intestine (qualitative assessment by two independent observers: *Ndrg4*$^{-/-}$ intestine: Nid1 and Fbln2 = 2x ++ and 1x + versus *Ndrg4*$^{+/+}$ intestine: Nid1 = 1x + and 2x −/+; Fbln2 = 3x +/−).

Soluble Nidogen-1 and Fibulin-2 stimulate the growth and migratory capacities of intestinal (tumor) cells

NID1 and FBLN2 associate with each other and/or other ECM components in the basement membrane: e.g., laminin, fibronectin, and β-integrin receptors, to ensure a stable cellular environment (Miosge *et al,* 2001; de Vega *et al,* 2009). Taken into account their role in controlling normal cellular growth, development, polarization, migration and invasion, both proteins have been implicated in several pathogenic processes, including neurological disorders and cancer (Walker *et al,* 2018). Consequently, we attempted to translate the above-described findings using human tissues and human *in vitro* cultures.

Similar as observed in mouse, NID1 and FBLN2 are highly expressed within the plexuses of the human ENS and a limited expression is observed within the epithelium (Fig 5A). To explore whether the combinatorial treatment of NID1&FBLN2 affects the proliferation speed of the normal human intestinal epithelium, we exposed normal human intestinal organoids (HIOs) to NID1&FBLN2 within their Matrigel® dome and observed a significantly enhanced relative growth rate of HIOs (Fig 5B, P = 0.012). Next, we assessed the influence of these ECM molecules on CRC cell proliferation (Fig 5C) and migration (Fig 5D) by administrating NID1&FBLN2 to the culture medium of HCT116 and Caco-2 CRC cells. Treating these cells with NID1&FBLN2 significantly enhanced HCT116 cell proliferation after 72 h (P = 0.044), but had no effect on the proliferation rate of Caco-2 cells (Fig 5C). NID1&FBLN2 had a stimulating effect on HCT116 and Caco-2 cell migration after 24 and 48 h, respectively (Fig 5D, P = 0.024 and P = 0.016, respectively).

Knowing that changes in the secretome are associated with various cancer types (Schaaij-Visser *et al,* 2013; Crotti *et al,* 2017; Robinson *et al,* 2019), we aimed to evaluate the clinical translatability of NID1 and FBLN2 by determining these protein levels in a cohort of matched human colonic normal and cancer tissue secretomes. Interestingly, in agreement with the positive correlation of NID1 expression with the mesenchymal subtype and more advanced

Figure 4. Nidogen-1 (Nid1) and Fibulin-2 (Fbln2) are highly present in the *Ndrg4*$^{-/-}$ ENS cell secretome and expressed within the ENS.

A Box plot showing the quantitative protein expression results of nanoLC-MS/MS analysis reveals the significantly higher presence of Nid1 and Fbln2 in the *Ndrg4*$^{-/-}$ compared to the *Ndrg4*$^{+/+}$ ENS cell secretome (n = 4; NSAF, normalized spectral abundance factor). Data are analyzed with R version 3.5.2 and the ibb R package. Each dot within the box plot represents the NSAF of an individual sample; the inside band reflects the median, and the bottom and top of the box the first and third quartile, respectively. The whiskers reflect the minimum and maximal values within 1.5× the interquartile range. NSAF values were compared using the Mann–Whitney U-test.

B Data derived from the Linnarsson mouse database (http://mousebrain.org/) display the expression of *Nid1* and *Fbln2* within cells of the central, peripheral, and enteric nervous system. Unit color scale: Expression (log(UMI)); UMI, unique molecular identifier. Abbreviations: ENS, enteric nervous system (i.e., enteric neurons and glial cells); OL, oligodendrocytes; Exc N, excitatory neurons in CNS; Hippo, hippocampus; MB, midbrain; HB, hindbrain; Str, striatum; Hyp, hypothalamus; BG, basal ganglia; OB, olfactory bulb; CB, cerebellum; SC, spinal cord; PNS, peripheral nervous system; Glia, glial cells; and Vasc, vasculature.

C–E Representative immunohistochemistry (C) and more detailed immunofluorescence (D, E) labeling indicate that Nid1 (C, D) and Fbln2 (C, E) are expressed within the myenteric plexus and by primary ENS cells ((C), n = 3, black arrowheads, scale bars, 50 μm; (D, E), n = 3, scale bars, 10 μm).

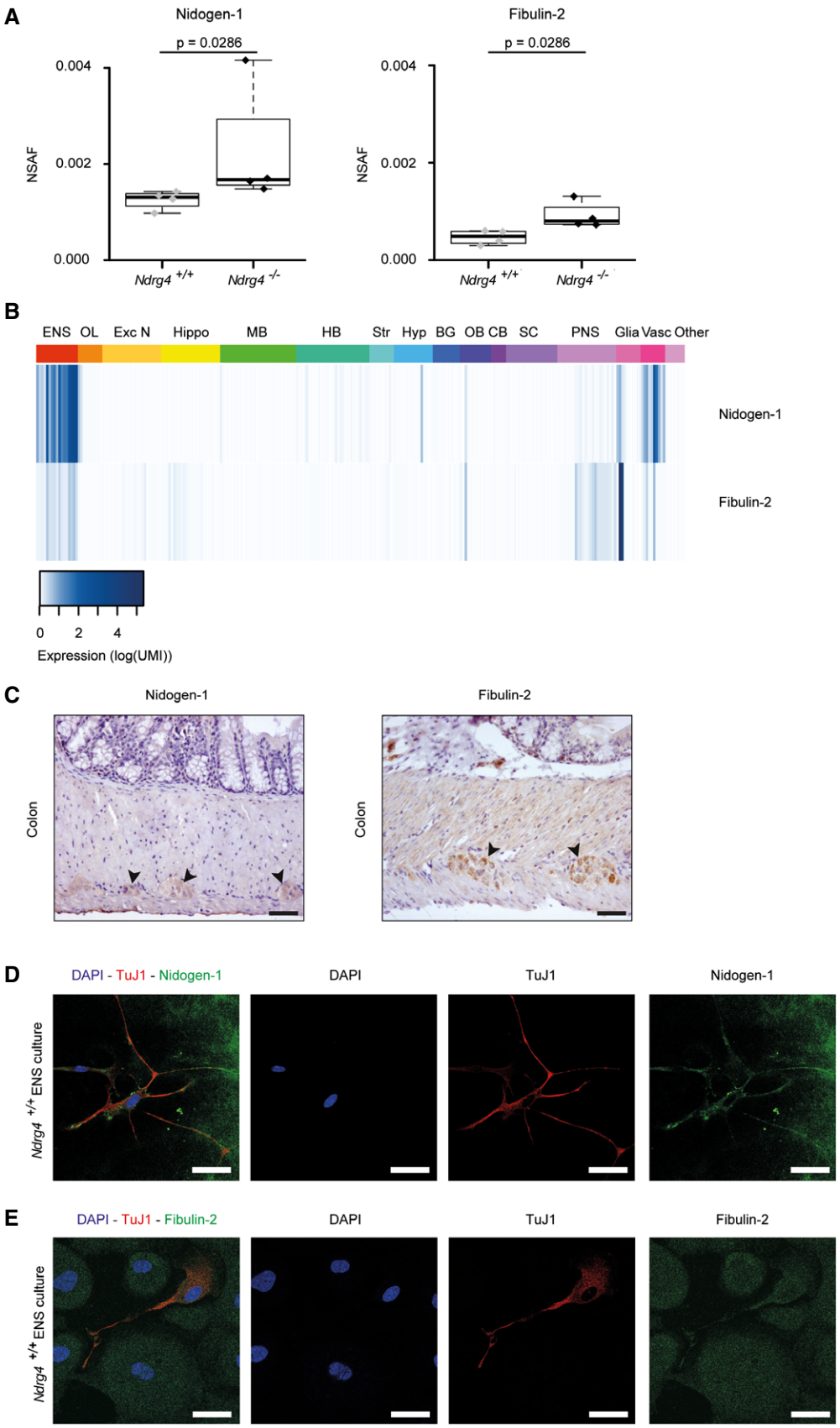

Figure 4.

CRC stages (Zhou *et al,* 2017; Rokavec *et al,* 2019), nanoLC-MS/MS analysis identified the significantly enriched presence of both NID1 and FLBN2 in CRC compared to normal secretomes (Fig 5E, $P < 0.0001$ for both). In line with the secretome data, we observed increased expression of both NID1 and FBLN2 within the cancerous epithelium (Fig 5F; $n = 3$; qualitative assessment; normal epithelium: NID1 = 2x −/+ and 1x +; FBLN2 = 3x +/− versus cancerous epithelium: NID1 and FBLN2 = 1x + and 2x ++).

The higher abundance of Nid1 and Fbln2 in the *Ndrg4*$^{-/-}$ ENS cell secretome (Fig 4A) suggests that Nid1 and Fbln2 are responsible for the enhanced IEO proliferation *in vitro* (Fig 3E–H), which is confirmed by the accelerated growth of HIOs after NID1&FBLN2

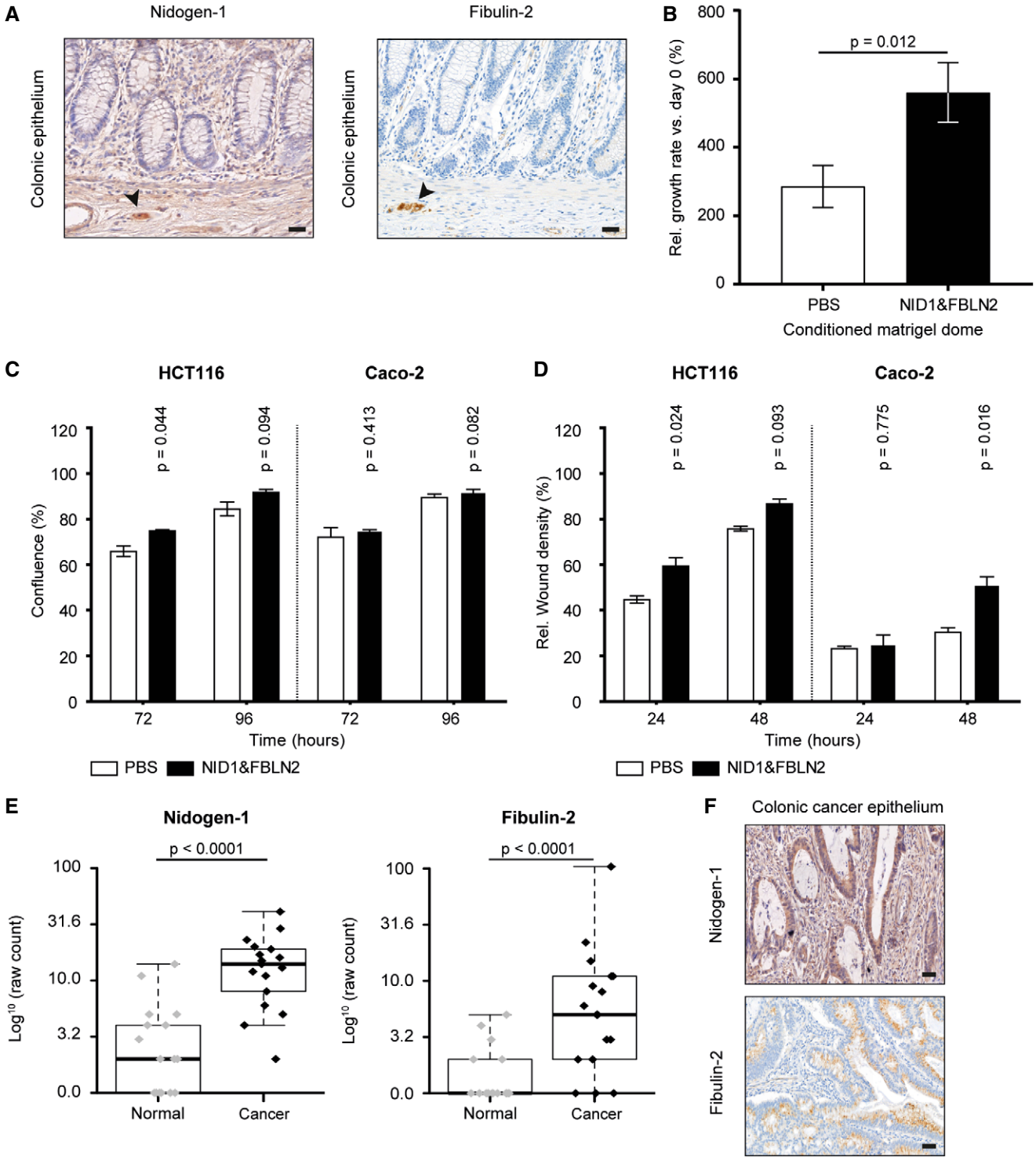

Figure 5.

Figure 5. NID1 and FBLN2 enhance HIO proliferation and CRC cell migration *in vitro* and are significantly up-regulated in the cancer tissue secretome.

A Representative microscopic views show that NID1 and FBLN2 are highly expressed in the human colonic ganglia (black arrowheads) and interconnecting nerve fibers, and in a limited level throughout the epithelium (n = 3). Scale bar, 50 μm.

B Addition of NID1&FBLN2 to the Matrigel® dome significantly enhanced the relative growth rate of HIOs after 5 days of culture as compared to the PBS control condition.

C Compared to the PBS control condition (white), stimulation with NID1&FBLN2 (black) enhanced the proliferation rate of HCT116 cells after 72 h, but did not affect Caco-2 cell proliferation.

D The migration rate of HCT116 cells was already significantly increased 24 h after addition of NID1&FBLN2 (black), whereas the migration of Caco-2 cells only significantly increased after 48 h of culture with NID1&FBLN2 (black).

E Box plot reflecting the quantitative nanoLC-MS/MS analysis results shows the up-regulation of NID1 and FBLN2 in the colorectal cancer tissue secretome (n = 17) compared to the normal colon tissue secretome (n = 17). Data are analyzed with R version 3.5.2 and the ibb R package. Within the box plots, each dot represents the log10-transformed raw count of an individual sample; the inside band is the median value; the bottom and top of the box the first and third quartile, respectively; and the whiskers reflect the minimum and maximal values within 1.5× the interquartile range.

F Representative images of human colonic cancer epithelium (n = 3) show a high scattered expression of NID1 and FBLN2 within the cancerous epithelium. Scale bar, 50 μm.

Data information: Data in (B) are derived from three independent experiments and represented as relative mean percentage ± SEM versus day 0, with the *P*-value determined using a two-tailed, unpaired *t*-test. Data in (C and D) are derived from three independent experiments and are represented as mean ± SEM, with *P*-values determined using a two-tailed, unpaired *t*-test. To compare the paired normal colon and CRC secretome data in (E) (n = 17), a paired Beta-Binominal test, taking into account the sample origin (i.e., comparing protein signatures between tissues derived from the same patient), was performed (Pham & Jimenez, 2012; de Wit *et al*, 2014). Source data are available online for this figure.

stimulation (Fig 5B) and in line with reports showing that NID1 and FBLN2 are able to activate the ERK/MAPK pathway (Zhang *et al,* 2014; Zhou *et al,* 2017). Moreover, with higher levels of NID1 and FBLN2 in mesenchymal-like (CRC) cells and the positive correlation between NID1 expression and mesenchymal-associated genes (Zhang *et al,* 2014; Zhou *et al,* 2017; Ibrahim *et al,* 2018; Tsuda, 2018; Rokavec *et al,* 2019), it is likely that Nid1 and Fbln2 drive CRC progression. Similar as in other cancers (Baird *et al,* 2013; Zhou *et al,* 2017; Ibrahim *et al,* 2018), our assays showed that NID1&FBLN2 especially enhance the migration rate of epithelial-like HCT116 and Caco-2 cells (Fig 5D), most likely via binding and activation of (one of) the abundantly present β-integrin receptor family members (Ahmed *et al,* 2003; Boudjadi *et al,* 2017). Recent evidence has shown that tumor cells are able to adhere to the ECM of myelinated peripheral nerves (Deborde *et al,* 2016) and that tumor epithelial cells bind to and migrate along enteric neurons through their interaction with N-cadherin (Duchalais *et al,* 2018). This interaction can cause β-catenin to translocate into the nucleus, thereby stimulating migration and invasion of CRC cells (Mrozik *et al,* 2018). Further studies are needed to identify which specific receptors are targeted by NID1 and FBLN2, e.g., β1-integrin receptors (Zhou *et al,* 2017; Ibrahim *et al,* 2018), and thereby mediate the observed effects in this study.

In summary, our data support our hypothesis that (in-)direct (paracrine) signaling from the ENS influences the pathogenesis of CRC (Rademakers *et al,* 2017). Given that remodeling of the TME can influence carcinogenesis (Crotti *et al,* 2017; Zahalka & Frenette, 2020), our data argue that the ENS and its signals are crucial components of the TME that may be targeted in future therapeutic strategies (Venkatesh, 2019; Zahalka & Frenette, 2020).

Materials and Methods

Patients

Formalin-fixed, paraffin-embedded human normal and cancerous colon tissues of CRC patients (n = 3) were retrospectively collected from the archive of the Department of Pathology of the Maastricht University Medical Center (MPTC: 2011-10 and 2015-12; Maastricht; The Netherlands). In addition, fresh tissue from patients that underwent surgical resection at the VU University Medical Center (Amsterdam; The Netherlands) was collected at the Department of Pathology and included for matched normal and CRC tissue secretome analysis (n = 17), as previously described (de Wit *et al,* 2014). Collection, storage and use of tissue and patient data were performed in compliance with the "Code for Proper Secondary Use of Human Tissue in the Netherlands" (https://www.federa.org/).

Human cell culture

The human CRC cell lines HCT116 and Caco-2 (LGC, Teddington, UK) were cultured as previously described (Melotte *et al,* 2009). Prior to utilization in experimental assays, cellular DNA was harvested and authenticated by short tandem repeat (STR) DNA typing (August 2019, Leibniz-Institute DSMZ-German Collection of Microorganisms and Cell cultures, Germany).

Proliferation and migration assay

To assess the influence of the two identified extracellular matrix (ECM) proteins, Nidogen-1 (NID1) and Fibulin-2 (FBLN2), on the proliferation and migration capacities of the human CRC cell lines HCT116 and Caco-2, a mixture of NID1 (2.0 μg/ml in PBS, 2570-ND-50, R&D systems) and FBLN2 (1.0 μg/ml in PBS, 9559-FB-050, R&D Systems) was added to the cell culture medium. To control for effects induced by PBS, proliferation and migration were also monitored upon addition of PBS (2.2%) to the cell culture medium. For the *proliferation assay*, 1,500 HCT116 and Caco-2 cells were seeded in a 96-well plate (3595, Corning® Costar®) and allowed to settle for 16 h under standard culture conditions (95% O_2/5% CO_2, 37°C). Cell proliferation was monitored by capturing images every 24 h for a maximum of five consecutive days (120 h). Cell confluence was determined using the Leica QWIN V3 software (custom-design by Dr. Ir. J. Cleutjens). Similarly, for the *migration assay*, 40,000 HCT116 and 25,000 Caco-2 cells were seeded in a 96-well plate (3595, Corning® Costar®) and allowed to grow under standard culture conditions (95% O_2/5% CO_2, 37°C). Sixteen hours later, a

700–800 μm wide scratch was made with the IncuCyte® Wound maker. Cell migration was monitored by capturing images every 24 h for a maximum of three consecutive days (72 h) and analyzed for wound width and relative wound density using the Leica QWIN V3 software (custom-design by Dr. Ir. J. Cleutjens).

Mice

Ndrg4 wild-type (*Ndrg4*$^{+/+}$) and knockout (*Ndrg4*$^{-/-}$) littermates, and *Ndrg4* floxed (*Ndrg4*$^{fl/fl}$) mice, kindly provided by Prof. Baldwin (Vanderbilt University Medical Center, Nashville; USA (Qu *et al,* 2016)), were on a mixed C57BL/6 genetic background (matching 59.7% C57BL/6NRj and 66.8% C57BL/6NRj, respectively; GVG Genetic Monitoring, Germany). *VillinCre* mice on the C57BL/6J genetic background (intestinal epithelial-specific Cre model) were kindly provided by Prof. Köhler (Maastricht University, Maastricht; The Netherlands). *APC*$^{Min/+}$ mice, also on a C57BL/6J background, which have a genetic predisposition to intestinal adenoma formation, were purchased from the Jackson Laboratory (002020, Bar Harbor; USA). Prior to experiments, all mice were characterized by genotyping PCR (Vaes *et al,* 2017), using the primer sequences listed in Table 1, Part A. Animals were age- and gender-matched and randomly housed in groups of 3–5 under standard conditions having free access to food and water. At the age of 13 weeks, *Ndrg4*$^{+/+}$ (n = 6–12) and *Ndrg4*$^{-/-}$ (n = 7–12) littermates were used for gastrointestinal motility assays as described below (Raffa *et al,* 1987; Nagakura *et al,* 1996). At the age of 12 months, *Ndrg4*$^{+/+}$ (n = 12) and *Ndrg4*$^{-/-}$ (n = 6) littermates were sacrificed and tissues collected for in-depth investigation by an experienced animal pathologist (MJG) blinded to the genotype. All animal experiments were approved by the Committee of Animal Welfare of Maastricht University and performed according to Dutch regulations.

Gastrointestinal motility assays

The whole-gut transit and small intestinal transit experiments were performed on two consecutive days because pairwise housing was required according to Dutch regulations. For both assays, mice were fasted for 1 h and subsequently administered 0.3 ml of 6% (w/v) carmine red dye (C1022, Sigma-Aldrich) in 0.5% (w/v)

Table 1. Primers sequences and annealing temperatures for (quantitative) PCR analysis.

Target	Forward primer	Reverse primer	Annealing temp.
Part A. Primers and annealing temperatures for genotyping PCR analysis			
NDRG4$^{+/-}$			
NDRG4 4HLOX1	TAGGCAGGGGCAGGTGGGTTTGT		60°C
NDRG4 4HLOX2		GGCGTCTCGATGTCATGTTCCTGT	60°C
NDRG4 4H776		GCTCCCACTCCAATGCCAATC	60°C
NDRG4$^{fl/fl}$			
NDRG4 4HLOX1	TAGGCAGGGGCAGGTGGGTTTGT		58°C
NDRG4 4HLOX2		GGCGTCTCGATGTCATGTTCCTGT	58°C
VillinCre			
Villin-Cre	GTGTGGGACAGAGAACAAACC	ACATCTTCAGGTTCTGCGGG	62°C
Wild-type	CAAATGTTGCTTGTCTGGTG	GTCAGTCGAGTGCACAGTTT	62°C
APC$^{Min/+}$			
APC wild-type	GCCATCCCTTCACGTTAG		53°C
APC common		TTCCACTTTGGCATAAGGC	53°C
APC mutant		TTCTGAGAAAGACAGAAGTTA	53°C
Part B: Primers and annealing temperatures for quantitative real-time PCR analysis			
Cyclo A (ppia)	CAAATGCTGGACCAAACACAA	TTCACCTTCCCAAAGACCACAT	60°C
Ndrg4-B	TCCGGGGCTCTCCCAAAGGG	GGCATCCACGTGGCACACCA	60°C
Vamp2	CTGCACCTCCTCCAAACCTTAC	TTCACCCTCATGATGTCCACC	62°C
Rabac1	TCTGGCTGTCTTCTTTGGCG	TACTGATGTGCTGGGCTCAC	60°C
Rab3a	CCACAGCCTATTACCGAGGC	GCACTGCATTAAATGACTCCTCA	60°C
Stx1a	TCACTGTCACTGTGGACCGA	CCTCCACGTTTTCGGCAATC	60°C
Stxbp1	ACCTCATCACCCCATCTGAG	CCGATATTTAGCAGTCGGCG	60°C
Snap25	ATCAGTGGTGGCTTCATCCG	CCTGCTCCAGGTTCTCATCC	62°C
Nsf	CTGTGCGGTTGTGAACGAAA	GGATGGGTCCTCAGCGTAAA	60°C
Cadps	AGCATGGAAATGGGCCAAGA	TTGCCACCAAAAGTGTGATCATT	62°C
Caly	CTGGCTTGCAGTCACTCAGA	CACAGCCCAGAAGTGCCATA	60°C

methylcellulose (M0512, Sigma-Aldrich) by oral gavage. The time period from gavage until the excretion of the first red-colored pellet was recorded as *total intestinal transit time* (Sasselli *et al,* 2013). Maximum observation time was 5 h. Mice who failed to expel a pellet were noted with a maximum transit time of 300 min. At the start of this 5 h course (9.00–10.00 am), mice were individually housed for 1 h in order to perform a stool analysis. All stools produced over this 1-h period were collected and subsequently desiccated at 75°C overnight to determine their dry weight. Water content per stool is expressed as the percentage of the difference between the wet and dry weight. For the small intestinal transit assay (Nagakura *et al,* 1996), mice were sacrificed 30 min after administration of the carmine red dye, whereafter the intestine was excised and the total length of the small intestine and the length travelled by the head of the red marker were measured. The *small intestinal transit* was expressed as the percentage of the distance travelled by the marker relative to the length of the small intestine. Distal colonic propulsion (Raffa *et al,* 1987) was determined by inserting a 2–3 mm glass bead 2 cm into the distal colon of each anesthetized (isoflurane) mouse twice, with 100 min recovery time in between. The *colonic propulsion time* was defined as the time from insertion till expulsion of the inserted glass bead.

Experimental models of colorectal cancer

$APC^{Min/+}$ mice (Heyer *et al,* 1999) were bred with (i) $Ndrg4^{+/-}$ or (ii) $Ndrg4^{fl/+}$-*VillinCre* mice and subsequently intercrossed to generate the following progeny for experimental purposes: (i) $Ndrg4^{+/+}$-$APC^{Min/+}$ and $Ndrg4^{-/-}$-$APC^{Min/+}$ mice (constitutive knockout model) or (ii) $Ndrg4^{fl/fl}$-$APC^{Min/+}$ *and* $Ndrg4^{fl/fl}$-*VillinCre*-$APC^{Min/+}$ mice (epithelial-specific knockout model). In addition, $Ndrg4^{+/+}$ and $Ndrg4^{-/-}$ mice (6–8 weeks of age) were injected intraperitoneally with the mutagen azoxymethane (AOM, A5486, Sigma-Aldrich) dissolved in sterile phosphate-buffered saline (10 μg/g bodyweight) once a week for six consecutive weeks (before 11.00 a.m.) (Neufert *et al,* 2007). Early development of adenomas was monitored in both models by the presence of blood in the stool and anus prolapses. At the age of six months or ten weeks after the final AOM injection, $APC^{Min/+}$ and AOM-treated mice, respectively, were sacrificed and tissues collected for histopathological investigation. Prior to collection and fixation of intestinal sections/Swiss rolls, the number and size of polyps were determined in longitudinally opened intestines under a dissecting microscope (10× magnification) with a micrometer ocular. All animal experiments were approved by the Committee of Animal Welfare of Maastricht University and performed according to Dutch regulations.

Immunohistochemistry

Paraffin sections (4 μm) of entire Swiss rolls and human colonic sections were stained with hematoxylin and eosin (H&E) or subjected to immunohistochemistry as previously described (Vaes *et al,* 2017) using either one of the following primary antibodies diluted in PBS/0.5% BSA/0.1% Tween (PBT): rabbit anti-human chromogranin A (1:500, A0430, Dako), rabbit anti-human lysozyme (1:5,000, A0099, Dako), rat anti-mouse Ki67 (1:50, M7249, Dako), rabbit anti-human PGP9.5 (1:200, Z5116, Dako), rabbit anti-human Lgr5 (1:30, Ab71225, Abcam), rabbit anti-mouse entactin/Nidogen-1 (Mouse, 1:2,000; human, 1:1,000, ab14511, Abcam), and rabbit anti-human Fibulin-2 (Mouse, 1:1,000; human, 1:2,000, PA5-75510, Thermo Fisher Scientific). Paraffin-embedded Swiss rolls were also stained with the endogenous alkaline phosphatase detection method (Vector® red alkaline phosphatase substrate kit, SK-5100, Vector Laboratories, Inc., Burlingame) following the manufacturer's instructions or by the periodic acid–Schiff–Diastase method (PAS+). Briefly, dewaxed and rehydrated tissue sections were treated with diastase, incubated with a fresh 1.0% periodic acid solution (10 min), washed in distilled water, incubated with Schiff reagent (20 min), rinsed in tap water, counterstained with hematoxylin, dehydrated and coverslipped. Finally, intestinal Swiss rolls were labeled with the monoclonal anti-human β-catenin antibody (Clone CAT-5H10, 1:1,000, Zymed-Invitrogen) using the Vector® M.O.M.™ Immunodetection kit (MKB-2213, Vector Laboratories, Inc.) according to the manufacturer's guidelines. For negative controls, primary antibodies were omitted from the sections. All images were acquired at RT using a Leica DM3000 microscope equipped with the Leica DFC320 camera (Leica Microsystems, Wetzlar, Germany) and the QWIN V3 software (Leica Windows-based image analysis kit, version 3), except for the slides labeled for β-catenin, which were scanned using the Pannoramic 250 Flash II (3DHISTECH, Hungary).

Morphometric analysis and intestinal histopathology

The number of positively stained cells per intervillus region or crypt was counted in three microscopic views (200× magnification) in $Ndrg4^{+/+}$ and $Ndrg4^{-/-}$ intestinal sections subjected to IHC (n = 3/4 per genotype) using the Leica QWIN V3 software. In addition, intestinal tumors in the experimental models of CRC were evaluated for their aggressive behavior using a semi-quantitative nuclear β-catenin scoring, according to Chung *et al* (Chung *et al,* 2001) and Wong *et al* (Wong *et al,* 2002). More precisely, the intensity of β-catenin positivity (0 = no expression, 1 = weak expression, 2 = moderate expression, 3 = strong expression, 4 = very strong expression) was determined separately in the membrane, cytoplasm, and nucleus for each intestinal tumor. The mean nuclear β-catenin score was expressed as the percentage of cells with a positively stained nucleus multiplied by the staining intensity (CaseViewer 1.4 software, 3DHISTECH).

Immunofluorescence and quantification of enteric neuron number

Immunofluorescence stainings were performed on primary ENS cell cultures and whole-mount colonic plexus preparations as previously described (Boesmans *et al,* 2015; Vaes *et al,* 2017) using the following primary antibodies: rabbit anti-NDRG4 (1:100, #9039, Cell Signaling), mouse anti-HuC/D (1:200, A21271, Thermo Fisher Scientific), mouse anti-TuJ1 (1:1,000, 801201, Biolegend), rabbit anti-S100 (undiluted, IS50430-2, Agilent), rabbit anti-Fibulin-2 (1:50, PA575510, Thermo Fisher Scientific), and rabbit anti-Entactin/Nidogen-1 (1:200, ab14511, Abcam), and secondary antibodies: donkey-anti-rabbit Alexa 488 (1:1,000, A21206, Thermo Fisher Scientific) and donkey-anti-mouse Alexa 594 (1:500, A21203, Thermo Fisher Scientific), diluted in blocking solution (4% donkey serum in PBS-0.5% Triton X). All cells and plexus preparations were mounted using Citifluor with or without DAPI (AF1/DAPI-15 and AF1,

Citifluor Ltd., Electron Microscopy Sciences) before imaging on a confocal Leica TCS SP8 microscope (25 × H_2O immersion lens for plexus preparations and 68 × oil immersion lens for primary cultures). For the quantification of the number of enteric neurons, two regions per colonic plexus preparation were imaged (surface area at least 1.0 mm^2/region) and the enteric neurons were manually counted using ImageJ (Cell Counter plugin) with observers blinded to genotype.

Primary (3D-) cultures

Primary ENS cell cultures were generated from the intestine of *Ndrg4*$^{+/+}$ and *Ndrg4*$^{-/-}$ mice as described (Lowette *et al,* 2014) with minor modifications. Tissue preparations of the longitudinal muscle with adherent myenteric plexus were isolated from the small intestine and collected in Krebs solution (mixture of NaCl, KCl, $MgCl2*6H_2O$, $NaH_2PO_4*1H_2O$, $NaHCO_3$ anh., glucose and $CaCl_2*2H_2O$; 95% O_2/5% CO_2; 4°C). After washing, tissue preparations were digested in a mixture of collagenase type II (11.34 mg/ml, 17101015, Thermo Fisher Scientific), dispase type II (1 mg/ml, 17105041, Thermo Fisher Scientific), BSA (5% in PBS, A7030, Sigma-Aldrich), and DNase I (4,000 μg/ml, 79254, Qiagen) for 8 min at 37°C. Krebs solution with 10% FBS was used to stop enzymatic digestion, and after washing by centrifugation (360 *g*, 8 min, 4°C), the pellet was resuspended in DMEM-F12 (31331-028, Thermo Fisher Scientific) enriched with 10% FBS, 1.0% glutamine, and 1.0% pen/strep (Lonza Group Ltd.). The cells (mixture containing neurons, glial cells and, e.g., smooth muscle cells and fibroblasts) were cultured in a 12-well plate at 37°C (95% O_2/5% CO_2). After 24 h, the medium was replaced by serum-free DMEM-F12 supplemented with 0.05% nerve growth factor (NGF, N-130, Alomone Laboratories), 0.2% N2 (17502-048, Invitrogen), and 0.02% G5 (17503-012, Invitrogen). The medium was changed every 2 days, and cells were cultured for a maximum of 7 days in order to prevent overgrowth of non-ENS cell types. At that point, cells were harvested (pool three wells of a 12-well plate) for further analysis.

For immunofluorescence experiments (Vaes *et al,* 2017), tissue preparations of the longitudinal muscle with adherent myenteric plexus were digested in a mixture of Krebs solution, collagenase type II (4,900 U), and 0.3 mg/ml BSA for 1 h at 37°C. After centrifugation (360 *g*, 8 min, 4°C), the cell pellet was resuspended in 0.05% trypsin in HBSS (without calcium) and incubated for 7 min at 37°C. Neutralizing medium (DMEM/F12 with 10% FCS and 1.0% pen/strep) was used to stop the enzymatic reaction. The cell pellet was resuspended in neuronal medium (Neurobasal™ plus medium (A3582901, Thermo Fisher Scientific) enriched with 2.0% B-27 (17504044, Thermo Fisher Scientific), 1.0% FCS, 2 mM glutamax (11574466, Thermo Fisher Scientific), 10 ng/ml GDNF (GFM37-10, Cell Guidance Systems), and 1.0% pen/strep) and filtered through a 40-μm cell strainer, where after the cells were plated onto laminin (L2020, Sigma-Aldrich)/poly-D-lysine (P7280, Sigma-Aldrich)-coated coverslips in a 12-well plate at 37°C (95% O_2/5% CO_2). Half of the medium was changed every 2 days, and cells were fixed after 5 days of culture with 4% formaldehyde.

Primary intestinal epithelial organoids (IEOs) were generated from the small intestine of wild-type mice according to *STEMCELL™ Technologies* instructions with slight adaptations. The isolated intestinal segment was flushed with cold PBS and cut open longitudinally. After washing the lumen, the segment was cut into 2 mm pieces that were systematically rinsed with cold PBS until the supernatant became clear. The pieces were dissociated (2 mM EDTA/PBS, shaking, 15 min) and resuspended in PBS/10% FBS, followed by collection of the supernatant through a 70-μm filter, which was repeated three times. The intestinal crypts were pelleted by three centrifugation steps (290 *g*, 5 min, 4°C), resuspended in 1:1 IntestiCult™ Organoid Growth Medium (OGM, 06005, STEMCELL™ Technologies)/undiluted Matrigel® (BD356231, Corning®), and carefully pipetted in the center of a pre-warmed 24-well plate. After solidification of the Matrigel® (±20 min, 37°C), OGM supplemented with 1.0% pen/strep was added to the crypts and the plate incubated at 37°C (95% O_2/5% CO_2) to allow IEO growth. The medium was changed every 2 days. One day prior to experiments, the IEOs were disaggregated by gentle disruption of the Matrigel® dome with advanced DMEM-F12 (12634-010, Thermo fisher Scientific), pelleted (400 *g*, 5 min, 4°C), and gently resuspended in Matrigel® for culture.

Primary human intestinal organoids (HIOs) were kindly provided by the group of Dr. T.G.A.M. Wolfs (METC 16-4-185). Similar as described for the murine IEOs, HIOs were cultured in 1:1 human OGM/undiluted Matrigel® in the center of a 24-well plate, with refreshment of the medium every 2 days. Prior to experiments, the HIOs were disaggregated by gentle disruption of the Matrigel® dome with trypsin and incubation for ± 2 min at 37°C. After pelleting (400 *g*, 5 min, 4°C), the HIOs were resuspended in either one of the following conditioned Matrigel® domes: i.e., (1) 1:1 Matrigel®/Human OGM, (2) 1:1 Matrigel®/PBS, or (3) 1:1 Matrigel®/NID1/FBLN2 (both at a final concentration of 50 μg/ml) to assess the influence of NID1/FBLN2 on the growth rate of HIOs.

Western blotting

Protein isolation and Western blot analysis of ENS cells was done as previously described (Vaes *et al,* 2017) using the following antibodies: rabbit anti-human NDRG4 (1:1,000, #9039, Cell Signaling) and mouse anti-eIF4E (Loading control, Clone 87, 1:1,000, e27620, BD Transduction Laboratories).

RNA isolation and quantitative real-time PCR (qRT–PCR)

Total RNA was isolated from primary mouse ENS cells (derived and cultured as described in the primary (3D)-cultures paragraph) using TRIzol® reagent and the purelink RNA Mini Kit (Ambion, Life Technologies) according to the manufacturer's instructions. Possible genomic DNA contaminations were eliminated by on-column DNase treatment (RNase-Free DNase set, 79254, Qiagen). cDNA was synthesized from 1.0 μg of total RNA with the iScript cDNA synthesis kit (Bio-Rad). To determine changes in gene expression, qRT–PCR was performed on a CFX96 Real-Time PCR System using the SYBR Green detection method (iQ™ SYBR® Green Supermix, Bio-Rad Laboratories) and the following conditions: 10 min at 95°C, 40 cycles of 15 s at 95°C, and 45 s at 60°C, followed by 1 min at 95°C, 5 s at 65°C, and 95°C. The PCR (total of 12 μl) contained 24 ng cDNA, 1 × SYBR Green Supermix, and 800 nM of the forward and reverse primer. Data were analyzed using the Bio-Rad CFX manager 2.0 software (Bio-Rad Laboratories). Relative mRNA expression was calculated using the ΔC_t method, with the expression of each target gene normalized to the expression of the control gene cyclophilin A (Cyclo A). Primer

sequences listed in Table 1, Part B were designed using Primer blast and gene runner and manufactured by Eurogentec.

Co-culture systems and live cell imaging

To evaluate a possible influence of ENS cells on IEOs, we performed three independent, indirect co-culture experiments using primary ENS cells and IEOs. Medium derived daily from *Ndrg4*$^{+/+}$ and *Ndrg4*$^{-/-}$ ENS cultures was added for five consecutive days onto a transwell insert (6.4 mm transwell with 1 μm pore transparent polyethylene terephthalate (PET) membrane, 353504, BD Biosciences) that was placed on top of IEOs in a 24-well transwell carrier plate (353504, BD Biosciences). To monitor changes in IEO expansion and phenotype over time (days 0–5), ±35 IEOs per experimental condition were imaged every day with the Leica DM3000 microscope (100× magnification). Survival, relative growth rate, and proliferation of IEOs were evaluated microscopically. The relative growth rate was determined by measuring the circumference of the IEOs at day 0 and day 5 using the Leica QWIN V3 software (custom-design by Dr. Ir. J. Cleutjens). Proliferation was assessed by counting the newly formed buds per IEO (two independent researchers). In addition, IEO morphology (i.e., crypt, sphere, (budding) enterosphere, enteroid, microadenoma-like, non-viable structure) was assessed at days 0 to 5 by two independent researchers. Similarly, HIO expansion was monitored daily for five consecutive days, starting immediately after solidification of the conditioned Matrigel® dome using the Leica DM3000 microscope (100× magnification). Relative growth rate was determined by measuring the circumference of the HIOs (ImageJ).

Collection and processing of secretomes

Serum-free medium containing the secreted proteins was collected from ten 12 wells after 3 days of culture (60-70% confluence) to obtain the "ENS cell secretome" (n = 4 independent experiments). The medium was centrifuged (1,000 *g*, 5 min, RT) to remove detached cells and subsequently concentrated from approximately 10 ml to about 200 μl using a 3 KDa MWCO centrifugal concentrator (Amicon® UFC900324, Merck Millipore; 4,000 *g*, 60 min, RT). The ENS cell secretome was stored at −80°C until further use. Prior to proteomics analysis, the ENS cell secretomes were processed till digested peptides. In detail, proteins were precipitated using methanol/chloroform precipitation (Wessel & Flugge, 1984). Next, precipitated proteins were dissolved in 150 μl 50 mM Tris/HCl (pH 8.0) and 0.5% sodium deoxycholate (SDC) and digested overnight at 37°C with trypsin. The digest was acidified by adding trifluoroacetic acid (TFA) to a concentration of 0.5% to precipitate the detergent. SDC was then removed by centrifugation. Peptide digests were desalted on C18 stagetips (Rappsilber *et al,* 2007) and dried by vacuum centrifugation.

The (tumor) tissue secretomes (n = 17) were collected and processed as previously described (Locker *et al,* 2006; Piersma *et al,* 2010; de Wit *et al,* 2014).

NanoLC-MS/MS analysis of secretomes

For the ENS cell secretomes, all LC–MS/MS analyses were performed on a Q Exactive Plus mass spectrometer (Thermo Fisher Scientific, San Jose, CA). Dried peptide samples were resuspended in 0.5% formic acid in 2.0% acetonitrile and loaded onto an in-house made 30 cm × 75μm ID column filled with CSH130 C18 2.5 μm particles (Waters). Peptides were separated using an Easy NanoLC 1000 (Thermo Fisher Scientific, buffer A = 0.1% formic acid and buffer B = 0.1% formic acid in acetonitrile) using a gradient of 0-28% buffer B for 120 min, with a flow rate of 300 nl/min. Each data collection cycle consisted of 1 full MS scan (375–1,400 m/z) followed by 10 data-dependent MS/MS scans. Peak lists were automatically created from raw data files using the Mascot Distiller software (version 2.3, MatrixScience). The Mascot search algorithm (version 2.2, MatrixScience) was used for searching against the UniProt protein sequence database (taxonomy: *Mus musculus*, version: November 2017). The peptide tolerance was set to 10 ppm, and the fragment ion tolerance was set to 20 ppm. A maximum number of two missed cleavages by trypsin were allowed, and carbamidomethylated cysteine and oxidized methionine were set as fixed and variable modifications, respectively. The Mascot score cut-off value for a positive protein hit was set to 65. Individual peptide MS/MS spectra of single peptide hits with Mascot scores below 40 were checked manually and either interpreted as valid identifications or discarded. Typical contaminants, also present in immunopurifications using beads coated with pre-immune serum or antibodies directed against irrelevant proteins, were omitted.

The preparation and subsequent nanoLC-MS/MS analysis of human (tumor) tissue secretomes was performed similarly as described before (Celis *et al,* 2004; de Wit *et al,* 2014). In brief, CRC and adjacent normal colon tissue was cut into cubes of approximately 1 mm^3 and incubated in 100 μl PBS for 1 h at 37°C. The soluble fractions, referred to as "tissue secretome", were processed for LC–MS/MS analyses on a Q Exactive Plus mass spectrometer (Thermo Fisher Scientific, San Jose, CA). The UniProt protein sequence database (taxonomy: *Homo Sapiens*, version: November 2017) was used for protein identification.

Statistical analysis

Experimental *in vivo* and *in vitro* data were analyzed by a two-tailed, unpaired *t*-test (n > 3) or Mann–Whitney *U*-test (n = 3) for the comparison of the mutant (*Ndrg4*$^{-/-}$) and wild-type (*Ndrg4*$^{+/+}$) group. Differences between the number of *Ndrg4*$^{+/+}$ and *Ndrg4*$^{-/-}$ mice developing polyps were assessed using chi-square statistics with Yates correction. Differences in the number of intestinal organoids evolving to non-viable structures were evaluated with logistic regression analysis.

A quantitative differential protein expression analysis was performed between the mass spectrometry data of the *Ndrg4*$^{-/-}$ and *Ndrg4*$^{+/+}$ ENS cell secretome (n = 4) by calculating the normalized spectral abundance factors (NSAF) (Paoletti *et al,* 2006) for all proteins and samples. NSAF values were compared using the Mann–Whitney *U*-test. For the comparison between the paired normal colon and CRC secretome data (n = 17), a paired Beta-Binominal test, taking into account the sample origin (i.e., comparing protein signatures between tissues derived from the same patient) was performed (Pham & Jimenez, 2012; de Wit *et al,* 2014).

Murine and human secretome processing and statistical analyses were performed with the statistical programming language R version 3.5.2 (https://www.r-project.org/) and the ibb R package (Pham & Jimenez, 2012).

Differences in the proliferation and migration rate were assessed between groups at singular time-points using a one-way ANOVA and Dunnett post hoc test to compare each treatment with the PBS control condition.

Unless stated otherwise, all data were analyzed using IBM SPSS statistics 25, represented as mean ± SEM, and considered statistically significant at $P < 0.050$.

Data availability

The mass spectrometry proteomics data of the murine ENS secretome have been deposited to the ProteomeXchange Consortium via the PRIDE (Perez-Riverol *et al,* 2019) partner repository with the dataset identifier PXD024502. Human proteomics data of NID1 and FBLN2 are attached to this manuscript in a source data excel and PDF file: "Source proteomics data NID1&FBLN2 human normal and CRC secretome" and "Source annotated MSMS spectra NID1&FBLN2", respectively.

Expanded View for this article is available online.

Acknowledgements
We are grateful to Dr. Ir. J. Cleutjens for the custom-made program in the Leica QWIN V3 software for measuring IEO circumference, cell confluence, and relative wound density. We thank I. de Lange, a PhD student within the group of Dr. T.G.A.M. Wolfs for her technical support to set up our IEO and HIO cultures. We are highly appreciative of Ir. K. Bezstarosti for his support with the murine proteomics analysis and Dr. S. Piersma and Dr. A. Henneman for generating the source data files containing the human NID1&FBLN2 proteomics data. We are profoundly thankful to Dr. M.H.F.M. Lentjes for the help with the characterization of the *Ndrg4*$^{-/-}$ mouse and to K.L.J. Daenen and K.A.D. Wouters for their assistance with sectioning of intestinal tissues and the performance of immunostainings. The schematic figure file in our synopsis was created with BioRender.com. This work was financially supported by the KWF Kankerbestrijding grant (UM 2013-6075) and VENI-NWO grant (016.186.124) obtained by Dr. V. Melotte, and by the VIDI-NWO grant (016.196.367) obtained by Dr. W. Boesmans. Further support was granted by the VUmc Cancer Center Amsterdam for the proteomics infrastructure.

Author contributions
Study concept and design: NV and VM. Acquisition of data: NV, SLS, GR, AMH, MdW, AK, MJG, TGK, LM, EvdB, JD, KMAR. Bioinformatics analysis: AK and SLS. Statistical analysis: NV, MdW, AK, KMS, WB and KMAR. Pathological experiments: NV, SLS, GR, AMH, MdW, MJG, DWT, RJAF, CRJ and VM. Data interpretation: NV, SLS, GR, MdW, AK, MJG, DWT, RJAF, CRJ, PVB, WB, KMS, KMAR, RMWH and VM. Drafting of manuscript: NV and VM. Technical and/or material support: MDW, TGK, JRMVM, EvdB, TGAMW, DWT, JD, PVB, WB, KMAR, RMWH. Study supervision: VM. All authors critically reviewed the manuscript.

Conflict of interest
The authors declare that they have no conflict of interest.

References

Ahmed N, Oliva K, Wang Y, Quinn M, Rice G (2003) Downregulation of urokinase plasminogen activator receptor expression inhibits Erk signalling with concomitant suppression of invasiveness due to loss of uPAR-beta1 integrin complex in colon cancer cells. *Br J Cancer* 89: 374 – 384

Akbareian SE, Nagy N, Steiger CE, Mably JD, Miller SA, Hotta R, Molnar D, Goldstein AM (2013) Enteric neural crest-derived cells promote their migration by modifying their microenvironment through tenascin-C production. *Dev Biol* 382: 446 – 456

Albo D, Akay CL, Marshall CL, Wilks JA, Verstovsek G, Liu H, Agarwal N, Berger DH, Ayala GE (2011) Neurogenesis in colorectal cancer is a marker of aggressive tumor behavior and poor outcomes. *Cancer* 117: 4834 – 4845

Ayala GE, Dai H, Powell M, Li R, Ding Y, Wheeler TM, Shine D, Kadmon D, Thompson T, Miles BJ *et al* (2008) Cancer-related axonogenesis and neurogenesis in prostate cancer. *Clin Cancer Res* 14: 7593 – 7603

Baird BN, Schliekelman MJ, Ahn YH, Chen Y, Roybal JD, Gill BJ, Mishra DK, Erez B, O'Reilly M, Yang Y *et al* (2013) Fibulin-2 is a driver of malignant progression in lung adenocarcinoma. *PLoS One* 8: e67054

Bapat AA, Hostetter G, Von Hoff DD, Han H (2011) Perineural invasion and associated pain in pancreatic cancer. *Nat Rev Cancer* 11: 695 – 707

Benesh EC, Miller PM, Pfaltzgraff ER, Grega-Larson NE, Hager HA, Sung BH, Qu X, Baldwin HS, Weaver AM, Bader DM (2013) Bves and NDRG4 regulate directional epicardial cell migration through autocrine extracellular matrix deposition. *Mol Biol Cell* 24: 3496 – 3510

Boesmans W, Lasrado R, Vanden Berghe P, Pachnis V (2015) Heterogeneity and phenotypic plasticity of glial cells in the mammalian enteric nervous system. *Glia* 63: 229 – 241

Boudjadi S, Bernatchez G, Sénicourt B, Beauséjour M, Vachon PH, Carrier JC, Beaulieu JF (2017) Involvement of the integrin α1β1 in the progression of colorectal cancer. *Cancers* 9: 96

Celis JE, Gromov P, Cabezon T, Moreira JM, Ambartsumian N, Sandelin K, Rank F, Gromova I (2004) Proteomic characterization of the interstitial fluid perfusing the breast tumor microenvironment: a novel resource for biomarker and therapeutic target discovery. *Mol Cell Proteomics* 3: 327 – 344

Chung GG, Provost E, Kielhorn EP, Charette LA, Smith BL, Rimm DL (2001) Tissue microarray analysis of beta-catenin in colorectal cancer shows nuclear phospho-beta-catenin is associated with a better prognosis. *Clin Cancer Res* 7: 4013 – 4020

Colangelo T, Polcaro G, Muccillo L, D'Agostino G, Rosato V, Ziccardi P, Lupo A, Mazzoccoli G, Sabatino L, Colantuoni V (2017) Friend or foe? The tumour microenvironment dilemma in colorectal cancer. *Biochim Biophys Acta Rev Cancer* 1867: 1 – 18

Crotti S, Piccoli M, Rizzolio F, Giordano A, Nitti D, Agostini M (2017) Extracellular Matrix and colorectal cancer: how surrounding microenvironment affects cancer cell behavior? *J Cell Physiol* 232: 967 – 975

Deborde S, Omelchenko T, Lyubchik A, Zhou Y, He S, McNamara WF, Chernichenko N, Lee SY, Barajas F, Chen CH *et al* (2016) Schwann cells induce cancer cell dispersion and invasion. *J Clin Invest* 126: 1538 – 1554

Dehmer JJ, Garrison AP, Speck KE, Dekaney CM, Van Landeghem L, Sun X, Henning SJ, Helmrath MA (2011) Expansion of intestinal epithelial stem cells during murine development. *PLoS One* 6: e27070

Duchalais E, Guilluy C, Nedellec S, Touvron M, Bessard A, Touchefeu Y, Bossard C, Boudin H, Louarn G, Neunlist M *et al* (2018) Colorectal cancer cells adhere to and migrate along the neurons of the enteric nervous system. *Cell Mol Gastroenterol Hepatol* 5: 31 – 49

Fernandez Vallone V, Leprovots M, Ribatallada-Soriano D, Gerbier R, Lefort A, Libert F, Vassart G, Garcia MI (2020) LGR5 controls extracellular matrix production by stem cells in the developing intestine. *EMBO Rep* 21: e49224

Fontenas L, De Santis F, Di Donato V, Degerny C, Chambraud B, Del Bene F, Tawk M (2016) Neuronal Ndrg4 is essential for nodes of ranvier organization in zebrafish. *PLoS Genet* 12: e1006459

Furness JB (2012) The enteric nervous system and neurogastroenterology. *Nat Rev Gastroenterol Hepatol* 9: 286 – 294

Gutting T, Burgermeister E, Hartel N, Ebert MP (2018) Checkpoints and beyond - Immunotherapy in colorectal cancer. *Semin Cancer Biol* 55: 78 – 89

Hayakawa Y, Sakitani K, Konishi M, Asfaha S, Niikura R, Tomita H, Renz BW, Tailor Y, Macchini M, Middelhoff M *et al* (2017) Nerve growth factor promotes gastric tumorigenesis through aberrant cholinergic signaling. *Cancer Cell* 31: 21 – 34

Heyer J, Yang K, Lipkin M, Edelmann W, Kucherlapati R (1999) Mouse models for colorectal cancer. *Oncogene* 18: 5325 – 5333

Ibrahim AM, Sabet S, El-Ghor AA, Kamel N, Anis SE, Morris JS, Stein T (2018) Fibulin-2 is required for basement membrane integrity of mammary epithelium. *Sci Rep* 8: 14139

Imperiale TF, Ransohoff DF, Itzkowitz SH, Levin TR, Lavin P, Lidgard GP, Ahlquist DA, Berger BM (2014) Multitarget stool DNA testing for colorectal-cancer screening. *N Engl J Med* 370: 1287 – 1297

Kamiya A, Hayama Y, Kato S, Shimomura A, Shimomura T, Irie K, Kaneko R, Yanagawa Y, Kobayashi K, Ochiya T (2019) Genetic manipulation of autonomic nerve fiber innervation and activity and its effect on breast cancer progression. *Nat Neurosci* 22: 1289 – 1305

Kim JT, Kim JW, Kang YH, Kim KD, Lee SJ, Choi SC, Kim KS, Chae SK, Kim JW, Lim JS *et al* (2012) NDRG2 and PRA1 interact and synergistically inhibit T-cell factor/beta-catenin signaling. *FEBS Lett* 586: 3962 – 3968

Knijn N, Mogk SC, Teerenstra S, Simmer F, Nagtegaal ID (2016) Perineural invasion is a strong prognostic factor in colorectal cancer: a systematic review. *Am J Surg Pathol* 40: 103 – 112

Locker GY, Hamilton S, Harris J, Jessup JM, Kemeny N, Macdonald JS, Somerfield MR, Hayes DF, Bast RC (2006) ASCO 2006 update of recommendations for the use of tumor markers in gastrointestinal cancer. *J Clin Oncol* 24: 5313 – 5327

Lorenzi F, Babaei-Jadidi R, Sheard J, Spencer-Dene B, Nateri AS (2016) Fbxw7-associated drug resistance is reversed by induction of terminal differentiation in murine intestinal organoid culture. *Mol Ther Methods Clin Dev* 3: 16024

Lowette K, Tack J, Vanden Berghe P (2014) Role of corticosterone in the murine enteric nervous system during fasting. *Am J Physiol Gastrointest Liver Physiol* 307: G905 – 913

Magnon C, Hall SJ, Lin J, Xue X, Gerber L, Freedland SJ, Frenette PS (2013) Autonomic nerve development contributes to prostate cancer progression. *Science* 341: 1236361

Margolis KG, Gershon MD (2016) Enteric neuronal regulation of intestinal inflammation. *Trends Neurosci* 39: 614 – 624

Melotte V, Lentjes MH, van den Bosch SM, Hellebrekers DM, de Hoon JP, Wouters KA, Daenen KL, Partouns-Hendriks IE, Stessels F, Louwagie J *et al* (2009) N-Myc downstream-regulated gene 4 (NDRG4): a candidate tumor suppressor gene and potential biomarker for colorectal cancer. *J Natl Cancer Inst* 101: 916 – 927

Melotte V, Qu X, Ongenaert M, van Criekinge W, de Bruine AP, Baldwin HS, van Engeland M (2010) The N-myc downstream regulated gene (NDRG) family: diverse functions, multiple applications. *FASEB J* 24: 4153 – 4166

Miosge N, Holzhausen S, Zelent C, Sprysch P, Herken R (2001) Nidogen-1 and nidogen-2 are found in basement membranes during human embryonic development. *Histochem J* 33: 523 – 530

Mrozik KM, Blaschuk OW, Cheong CM, Zannettino ACW, Vandyke K (2018) N-cadherin in cancer metastasis, its emerging role in haematological malignancies and potential as a therapeutic target in cancer. *BMC Cancer* 18: 939

Nagakura Y, Naitoh Y, Kamato T, Yamano M, Miyata K (1996) Compounds possessing 5-HT3 receptor antagonistic activity inhibit intestinal propulsion in mice. *Eur J Pharmacol* 311: 67 – 72

Nagy N, Barad C, Hotta R, Bhave S, Arciero E, Dora D, Goldstein AM (2018) Collagen 18 and agrin are secreted by neural crest cells to remodel their microenvironment and regulate their migration during enteric nervous system development. *Development* 145: dev160317

Neufert C, Becker C, Neurath MF (2007) An inducible mouse model of colon carcinogenesis for the analysis of sporadic and inflammation-driven tumor progression. *Nat Protoc* 2: 1998 – 2004

Obermayr F, Hotta R, Enomoto H, Young HM (2013) Development and developmental disorders of the enteric nervous system. *Nat Rev Gastroenterol Hepatol* 10: 43 – 57

Paoletti AC, Parmely TJ, Tomomori-Sato C, Sato S, Zhu D, Conaway RC, Conaway JW, Florens L, Washburn MP (2006) Quantitative proteomic analysis of distinct mammalian Mediator complexes using normalized spectral abundance factors. *Proc Natl Acad Sci USA* 103: 18928 – 18933

Perez-Riverol YCA, Bai J, Bernal-Llinares M, Hewapathirana S, Kundu DJ, Inuganti A, Griss J, Mayer G, Eisenacher M, Pérez E *et al* (2019) The PRIDE database and related tools and resources in 2019: improving support for quantification data. *Nucleic Acids Res* 47(D1): D442 – D450

Peterson SC, Eberl M, Vagnozzi AN, Belkadi A, Veniaminova NA, Verhaegen ME, Bichakjian CK, Ward NL, Dlugosz AA, Wong SY (2015) Basal cell carcinoma preferentially arises from stem cells within hair follicle and mechanosensory niches. *Cell Stem Cell* 16: 400 – 412

Pham TV, Jimenez CR (2012) An accurate paired sample test for count data. *Bioinformatics* 28: i596 – i602

Piersma SR, Fiedler U, Span S, Lingnau A, Pham TV, Hoffmann S, Kubbutat MH, Jimenez CR (2010) Workflow comparison for label-free, quantitative secretome proteomics for cancer biomarker discovery: method evaluation, differential analysis, and verification in serum. *J Proteome Res* 9: 1913 – 1922

Qu X, Li J, Baldwin HS (2016) Postnatal lethality and abnormal development of foregut and spleen in Ndrg4 mutant mice. *Biochem Biophys Res Commun* 470: 613 – 619

Rademakers G, Vaes N, Schonkeren S, Koch A, Sharkey KA, Melotte V (2017) The role of enteric neurons in the development and progression of colorectal cancer. *Biochim Biophys Acta* 1868: 420 – 434

Raffa RB, Mathiasen JR, Jacoby HI (1987) Colonic bead expulsion time in normal and mu-opioid receptor deficient (CXBK) mice following central (ICV) administration of mu- and delta-opioid agonists. *Life Sci* 41: 2229 – 2234

Rappsilber J, Mann M, Ishihama Y (2007) Protocol for micro-purification, enrichment, pre-fractionation and storage of peptides for proteomics using StageTips. *Nat Protoc* 2: 1896 – 1906

Robinson JL, Feizi A, Uhlen M, Nielsen J (2019) A systematic investigation of the malignant functions and diagnostic potential of the cancer secretome. *Cell Rep* 26: 2622 – 2635.e5

Rokavec M, Bouznad N, Hermeking H (2019) Paracrine induction of epithelial-mesenchymal transition between colorectal cancer cells and its

suppression by a p53/miR-192/215/NID1 Axis. *Cell Mol Gastroenterol Hepatol* 7: 783 – 802

Sasselli V, Boesmans W, Vanden Berghe P, Tissir F, Goffinet AM, Pachnis V (2013) Planar cell polarity genes control the connectivity of enteric neurons. *J Clin Investig* 123: 1763 – 1772

Schaaij-Visser TB, de Wit M, Lam SW, Jimenez CR (2013) The cancer secretome, current status and opportunities in the lung, breast and colorectal cancer context. *Biochim Biophys Acta* 1834: 2242 – 2258

Schonkeren SL, Massen M, van der Horst R, Koch A, Vaes N, Melotte V (2019) Nervous NDRGs: the N-myc downstream–regulated gene family in the central and peripheral nervous system. *Neurogenetics* 20: 173 – 186

Stopczynski RE, Normolle DP, Hartman DJ, Ying H, DeBerry JJ, Bielefeldt K, Rhim AD, DePinho RA, Albers KM, Davis BM (2014) Neuroplastic changes occur early in the development of pancreatic ductal adenocarcinoma. *Can Res* 74: 1718 – 1727

Tsuda T (2018) Extracellular interactions between fibulins and transforming growth factor (TGF)-β in physiological and pathological conditions. *Int J Mol Sci* 19: 2787

Vaes N, Lentjes MHFM, Gijbels MJ, Rademakers G, Daenen KL, Boesmans W, Wouters KAD, Geuzens A, Qu X, Steinbusch HPJ *et al* (2017) NDRG4, an early detection marker for colorectal cancer, is specifically expressed in enteric neurons. *Neurogastroenterol Motil* 29: e13095

Vaes N, Schonkeren SL, Brosens E, Koch A, McCann CJ, Thapar N, Hofstra RMW, van Engeland M, Melotte V (2018) A combined literature and in silico analysis enlightens the role of the NDRG family in the gut. *Biochim Biophys Acta* 1862: 2140 – 2151

de Vega S, Iwamoto T, Yamada Y (2009) Fibulins: multiple roles in matrix structures and tissue functions. *Cell Mol Life Sci* 66: 1890 – 1902

Venkatesh HS (2019) The neural regulation of cancer. *Science* 366: 965

Walker C, Mojares E, del Río Hernández A (2018) Role of extracellular matrix in development and cancer progression. *Int J Mol Sci* 19: 3028

Wessel D, Flugge UI (1984) A method for the quantitative recovery of protein in dilute solution in the presence of detergents and lipids. *Anal Biochem* 138: 141 – 143

de Wit M, Kant H, Piersma SR, Pham TV, Mongera S, van Berkel MP, Boven E, Ponten F, Meijer GA, Jimenez CR *et al* (2014) Colorectal cancer candidate biomarkers identified by tissue secretome proteome profiling. *J Proteomics* 99: 26 – 39

Wong SC, Lo ES, Lee KC, Chan JK, Hsiao WL (2004) Prognostic and diagnostic significance of beta-catenin nuclear immunostaining in colorectal cancer. *Clin Cancer Res* 10: 1401 – 1408

Wong SC, Lo SF, Lee KC, Yam JW, Chan JK, Wendy Hsiao WL (2002) Expression of frizzled-related protein and Wnt-signalling molecules in invasive human breast tumours. *J Pathol* 196: 145 – 153

Zahalka AH, Frenette PS (2020) Nerves in cancer. *Nat Rev Cancer* 20: 143 – 157

Zeisel A, Hochgerner H, Lonnerberg P, Johnsson A, Memic F, van der Zwan J, Haring M, Braun E, Borm LE, La Manno G *et al* (2018) Molecular architecture of the mouse nervous system. *Cell* 174: 999 – 1014.e22

Zhang H, Wu J, Dong H, Khan SA, Chu ML, Tsuda T (2014) Fibulin-2 deficiency attenuates angiotensin II-induced cardiac hypertrophy by reducing transforming growth factor-beta signalling. *Clin Sci* 126: 275 – 288

Zhao CM, Hayakawa Y, Kodama Y, Muthupalani S, Westphalen CB, Andersen GT, Flatberg A, Johannessen H, Friedman RA, Renz BW *et al* (2014) Denervation suppresses gastric tumorigenesis. *Sci Transl Med* 6: 250ra115

Zhou Y, Zhu Y, Fan X, Zhang C, Wang Y, Zhang L, Zhang H, Wen T, Zhang K, Huo X *et al* (2017) NID1, a new regulator of EMT required for metastasis and chemoresistance of ovarian cancer cells. *Oncotarget* 8: 33110 – 33121